International Journal of Solids and Structures 49 (2012) 3823–3837

Contents lists available at SciVerse ScienceDirect

International Journal of Solids and Structures

journal homepage: www.elsevier.com/locate/ijsolstr

The effect of interfacial shear strength on damping behavior of carbon nanotube reinforced composites

D.N. Savvas *, V. Papadopoulos, M. Papadrakakis

Institute of Structural Analysis and Antiseismic Research, National Technical University of Athens, 9 Iron Polytechneiou, Zografou Campus, Athens 15780, Greece

ARTICLE INFO

Article history:
Received 28 April 2012
Received in revised form 5 July 2012
Available online 26 September 2012

Keywords:
Multi-scale analysis
Carbon nanotubes
Nanocomposites
Finite element analysis
Bond-slip interface model
Viscoelastic polymer model
Stochastic CNT waviness

ABSTRACT

The effect of interfacial shear strength (ISS) on the mechanical and damping properties of carbon nanotube reinforced composites (CNT-RCs) is investigated in the present study using a multiscale simulation. The atomic lattice of CNTs is modeled with the modified molecular structural mechanics (MMSM) approach and reduced to an equivalent beam element (EBE) which is used as the basic building block for the construction of full length CNTs embedded in the polymer. Linear material properties are assigned to the EBEs, while a Maxwell–Wiechert material model is used for modeling the viscoelastic behavior of the polymer. The interfacial load transfer mechanism between the lateral surface of the carbon nanotube and the surrounding matrix is taken into account with a nonlinear bond-slip friction-type model. Finite element models of representative volume elements (RVEs) are constructed comprised of two independent meshes: a structured with solid elements for the matrix and a series of embedded EBEs for the full length CNTs inside the matrix. Straight as well as wavy CNTs are considered. In the case of wavy CNTs, random CNT geometries are generated using the spectral representation method with evolutionary power spectra (EPS) which are derived from processing scanning electron microscope (SEM) images. Stochastic average properties were derived with Monte Carlo simulation. The mechanical and damping properties of the CNT-RCs are assessed on the basis of sensitivity analyses with respect to various weight fractions and interfacial shear strength (ISS) values. Numerical results are presented, showing the significant effect of the ISS as well as the influence of CNT waviness on the damping behavior of CNT-RCs.

1. Introduction

In recent years carbon nanotubes (CNTs) have attracted a lot of interest due to their superior mechanical properties. Experimental measurements (Demczyk et al., 2002; Iijima, 1991; Salvetat et al., 1999; Yu et al., 2000; Treacy et al., 1996) verified by numerical simulations (Arroyo and Belytschko, 2004a; Chang and Gao, 2003; Jin and Yuan, 2003; Thostenson and Chou, 2003) have calculated the stiffness of carbon nanotubes in the order of 1 TPa while their tensile strength is measured at about 150 GPa. These significant mechanical properties as well as their high aspect ratio and low density make CNTs ideal reinforcing elements in composite nanostructured materials. Nevertheless, unlike conventional fiber-reinforced composites, CNTs, due to their small length scale, can interact with polymer chains only through weak van der Waals forces, usually having marginal influence on the mechanical properties of the nanocomposite. However, experimental evidence (Ramanathan et al., 2005; Velasco-Santos et al., 2003; Zhu et al., 2003) demonstrated that if functionalization techniques are applied on the surface of carbon nanotubes, higher interfacial shear strength (ISS) may be achieved leading to improved stiffness and damping properties of the CNT-RCs.

From the computational mechanics point of view, classic atomic computational approaches, such as ab initio calculation (Chandraseker and Mukherjee, 2007; Van Lier et al., 2000; Zhou et al., 2001), molecular dynamics (MD) simulation (Agrawal et al., 2008; Chen et al., 2007) and the equivalent continuum modeling (ECM) (Cheng et al., 2009; Hu et al., 2007; Nasdala and Ernst, 2005; Odegard et al., 2002) are among the most widely used theoretical approaches for the numerical simulation of CNTs. In spite of the recent advances in computer technology, ab initio calculations and MD simulations are still limited to an atomic-scale and femtosecond time-scale models. On the other hand, ECM approaches tend to be a more efficient modeling technique for simulating larger-scale systems or longer time spans. In principle, this approach transforms chemical bonds between atoms in molecular mechanics (MM) into a continuum model using the finite element method (FEM) and thus provides a link between molecular mechanics and continuum mechanics. Among the ECM methods, the molecular structural mechanics (MSM) approach has attracted great attention because of its simplicity and effectiveness. In MSM, the lattice of the CNTs is modeled as a space frame structure with

* Corresponding author. Tel.: +30 210 772 4158.
E-mail address: dimitriosavvas@yahoo.gr (D.N. Savvas).

0020-7683/$ - see front matter © 2012 Elsevier Ltd. All rights reserved.
http://dx.doi.org/10.1016/j.ijsolstr.2012.08.031

the C–C covalent bond between the atoms being represented by continuum round beam (Li and Chou, 2003a). In a modified version of the molecular structural mechanics approach (MMSM) different bending rigidities are assigned along the major and minor principal axes of the considered rectangular beam (Chen et al., 2010). The stiffness properties of these beams are based on interatomic-potentials and equivalence between structural and molecular energy quantities. A quadratic potential is often used to account for the linear interaction behavior of atoms, while the Morse potential is used to account for the nonlinearity of the interactions (Arroyo and Belytschko, 2004b; Li and Chou, 2003a; Tserpes et al., 2006).

For the modeling of CNT-RCs, various multiscale methods have been proposed to account for the coupling of different length scales involved and the corresponding phenomena taking place at the interface of the CNT-RCs constituents. Among them, concurrent and sequential approaches are the most widely applied (Qian et al., 2008; Wernik and Meguid, 2009). Concurrent multiscale methodologies try to combine MD and continuum methods, bridging the atomistic nano-scale to the continuum macro-scale. In these approaches, the solution of the atomistic problem provides the boundary conditions or kinematic constraints that must be imposed to the continuum problem. On the other hand, sequential approaches apply a length separation and the problem is solved progressively form the smallest scale passing information to its subsequent scale and onwards. Following the latter approach Odegard et al. (2002), modeled the CNT, the local polymer near the nanotube, and the CNT-polymer interface as an effective continuum fiber which retains the local molecular structure and bonding information, and serves as a means for linking the equivalent-continuum to the nanomechanics model. Other researchers followed similar formulations for the modeling of CNT-RC interface (Lu et al., 2008; Needleman et al., 2010; Tan et al., 2007). In Tserpes et al. (2008) CNTs are modeled with a MSM model bonded with a surrounding polymer, while in Georgantzinos et al. (2009) spring elements connecting the CNT atoms and the polymer chain molecules were used to model the interface through weak van-der-Waals interactions based on the Lenard–Jones potential.

In the present study, the effect of ISS on the mechanical and damping properties of CNT-RCs is investigated using a multiscale simulation. The atomic lattice of CNTs is modeled as space frame structure using the MMSM approach. However, as CNTs form "ropes" with lengths of the order of micro meters, the detailed modeling of their nanostructure leads to an enormous computational effort in the context of MMSM. For this reason the MMSM model is reduced to an equivalent beam element (EBE) which is used subsequently as the basic building block for the construction of full length CNTs at the micro-scale embedded in the polymer. Linear material properties are assigned to the EBEs, while a Maxwell–Wiechert material model is used for modeling the viscoelastic behavior of the polymer. The polymer considered is the poly-ether–ether-ketone (PEEK). The interfacial load transfer mechanism between the lateral surface of the CNT and the surrounding matrix is taken into account with a nonlinear bond-slip friction-type model. Finite element models of RVEs are constructed comprised by two independently discretized meshes: a structured mesh with solid elements for the matrix and a series of embedded 3D EBEs for the full length CNTs inside the matrix. The influence of straight as well as wavy CNTs is investigated. In the case of wavy CNTs, random CNT geometries are generated using the spectral representation method with evolutionary power spectra (EPS) which are derived from scanning electron microscope (SEM) images. Stochastic average properties were derived with Monte Carlo simulation. The mechanical and damping properties of the CNT-RCs are assessed on the basis of sensitivity analyses with respect to various weight fractions in the range from 0.1% to 2% as well as to various ISS values ranging from very low values up to values larger than the shear strength of PEEK. Numerical results are presented, showing the significant effect of the ISS as well as the influence of CNT waviness on the damping behavior of CNT-RCs. A schematic representation of the adopted multiscale approach is illustrated in Fig. 1.

2. Modeling of carbon nanotubes

A single wall CNT (SWCNT) can be visualized as a tubular structure which can be constructed by rolling up a graphene sheet. According to the chirality of their atomic lattice, CNTs are grouped into armchair, zigzag and chiral nanotubes. Multiwall CNTs (MWCNTs) are constructed by co-axially situated SWCNTs with different radii, which are connected to each other by weak van der Waals forces. In the present study a MWCNT with an approximately outer diameter 14 nm is considered. Only the outer tube which is an armchair (100,100) nanotube is modeled using the MMSM approach. The reason for this simplification in the nanotube's modeling is that the effect of the inner tube layers on the mechanical properties of the MWCNT is slightly noticeable and becomes minor as the diameter of the tubes increases (Li and Chou, 2003b). In addition, the paper focuses on the effect of the ISS on the damping properties of the RVE, which means that only the lateral surface of the outer tube is important. The load transfer from polymer to the nanotube is totally accomplished through the outer tube's surface as the inner tubes are sliding on each other due to their weak interactions. However modeling of the inner layers of the MWCNT is required when vibrational characteristics and especially the "breathing" modes of the nanotubes are studying (Cheng et al., 2010).

2.1. Modified molecular structural mechanics

In the context of MMSM approach the C–C bonds of the atomic lattice of the nanotube are replaced by rectangular beam elements.

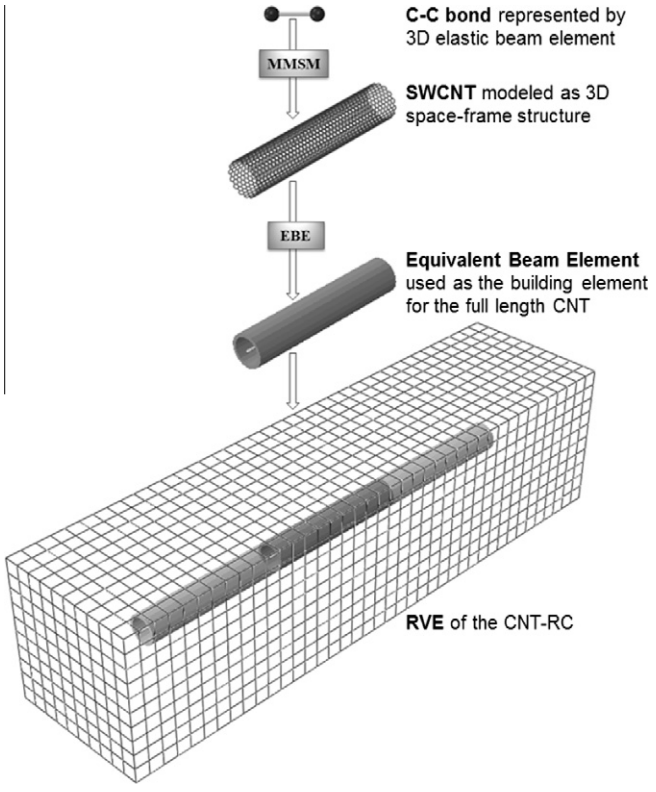

Fig. 1. Schematic representation of the multiscale RVE modeling.

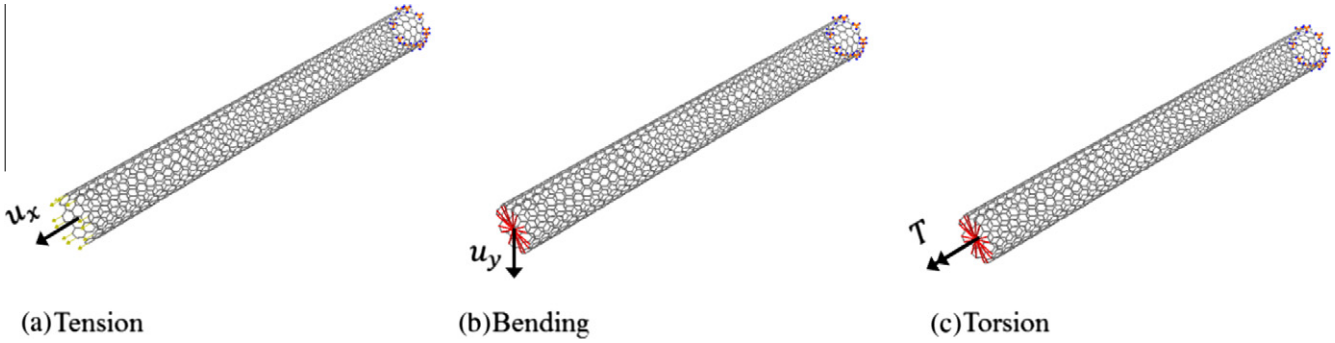

Fig. 2. FE mesh and boundary conditions for (a) Tension, (b) Bending and (c) Torsion loading on CNT model.

According to the potential energy of a covalent bond in molecular mechanics the beam bending rigidity is dependent on both the bond-angle variation energy and the inversion energy. More specifically, the inversion energy would mainly determine the bending stiffness of the covalent bond in the minor principal centroidal axis of the section while the bond-angle variation energy for that in the major one. Thus the following relationship between the structural mechanics parameters and molecular mechanics force field constants are derived:

$$k_r = \frac{EA}{L}, \quad k_\theta = \frac{E(I_y'' + I_z)}{L}, \quad k_\omega = \frac{3EI_y'}{L}, \quad k_\tau = \frac{GJ}{L} \tag{1}$$

$$I_y = I_y' + I_y'' = \left(\frac{k_\omega}{3k_\theta} + \tan\phi\right) I_z \tag{2}$$

Detailed explanations on the above equations can be found in Chen et al. (2010) where the modified MSM model was first presented.

2.2. Equivalent beam element (EBE) for CNTs

Although the MMSM approach overcomes the restrictions in time and size-scales that the MD method has, the detailed simulation of the nanostructure of a CNT results into a large-scale computational problem. For example a CNT with a diameter of 14 nm and 1 μm long corresponds to a numerical problem with degrees of freedom in the order of 10^7. Thus, the analysis of a CNT-RC containing even 1% weight fraction of CNTs is an extremely computationally demanding task. For this reason, the detailed MMSM model of the CNTs is reduced to an EBE with linear material properties. In order to derive the stiffness properties of the EBE, the detailed MMSM space frame model of CNT is subjected to three independent loading conditions, namely tension, bending and torsion. The boundary and loading conditions for each case are depicted in Fig. 2.

More specifically, the axial stiffness of the EBE is calculated by imposing an axial displacement u_x at one CNT's end simulated with a MMSM space frame of length L_0. The other end, in which the resulting reaction force F_x is calculated, is considered fixed (Fig. 2a). Thus, the axial stiffness can be calculated by

$$(EA)_{eq} = \frac{F_x L_0}{u_x} \tag{3}$$

For the bending case, a transverse displacement u_y is applied at the center point of one CNT's end where all nodes of this end are kinematically constrained as shown in Fig. 2b. The other CNT's end, where the resulting reaction force F_y is calculated by means of FE analysis, is considered fixed. The equivalent bending stiffness is then given by

$$(EI)_{eq} = \frac{F_y}{3u_y} L_0^3 \tag{4}$$

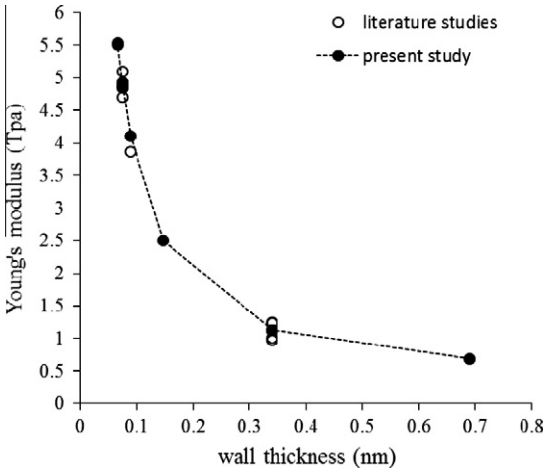

Fig. 3. Young's modulus of a pipe EBE for the armchair (8,8) CNT with respect to selected wall thickness values.

Similarly, for the torsion case, a torque T is applied at the center point of one CNT's end, which is kinematically constrained to the peripheral nodes of this section, as shown in Fig. 2c. The nodes at the other end section of the CNT are considered fixed. The angle of rotation φ of the center point is calculated by means of a FE analysis and the equivalent torsional stiffness of the EBE is calculated from

$$(GJ)_{eq} = \frac{T}{\phi} L_0 \tag{5}$$

In order to derive the elastic moduli from the calculated rigidities, a profile section for the EBE must be assumed. For instance, if a pipe profile is selected, its section properties are given by

$$A_{eq} = \frac{\pi}{4}\left[(d_{eq} + t)^2 - (d_{eq} - t)^2\right] \tag{6}$$

$$I_{eq} = \frac{\pi}{64} 2\left[(d_{eq} + t)^4 - (d_{eq} - t)^4\right] \text{and } J_{eq} = 2I_{eq} \tag{7}$$

where the equivalent diameter d_{eq} is calculated from the axial and bending rigidities, for an arbitrarily selected wall thickness value t of the hollow beam:

$$d_{eq} = \sqrt{8\frac{(EI)_{eq}}{(EA)_{eq}} - t^2} \tag{8}$$

Young's and shear moduli of the pipe EBE of an armchair (8,8) CNT, were computed by Eqs. (3)–(8) for different selected wall thickness values and compared to corresponding published results in the literature for various methodologies including MD, tight-binding

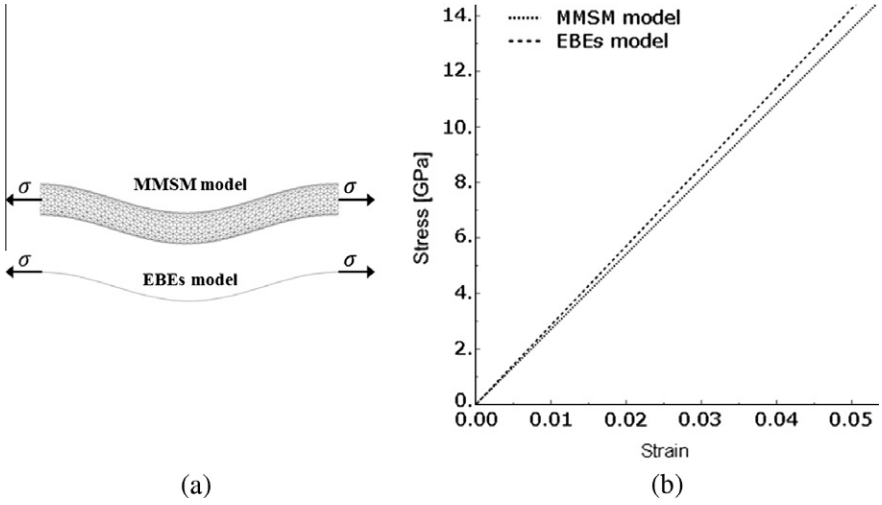

Fig. 4. (a) Curved MMSM model and corresponding series of EBE model, (b) Tensile stress strain curves.

models, ab initio computations and others (Jin and Yuan, 2003; Hernandez et al., 1998; Kudin et al., 2001; Li and Chou, 2003a; Lu, 1997; Odegard et al., 2002; Pantano et al., 2004; Tu and Ou-Yang, 2002; Yakobson et al., 1996; Zhou et al., 2000). Fig. 3 summarizes the results of the aforementioned comparison.

2.3. Validation of curved CNT EBEs model against MMSM model

In this section the ability of the EBE derived in the previous section, to predict the mechanical behavior of curved CNTs is demonstrated. For this purpose the predicted tensile mechanical behavior of a detailed curved MMSM model, which stands for a sinusoidal armchair (8,8) CNT, is compared to the corresponding prediction of a model constituted of a series of EBEs forming the same sinusoidal curve (Fig. 4a). The stress strain curves calculated with the above models are presented in Fig. 4b. From this figure it can be observed that the tensile elastic modulus extracted from the two models is almost the same with a difference of less than 5%.

3. Stochastic modeling of CNT waviness

Random CNT waviness is modeled as a non-homogeneous stochastic field using the spectral representation method in conjunction with evolutionary power spectra (EPS). The statistical properties of the EPS are derived from processing a number of CNT geometries from scanning electron microscope (SEM) images (Fig. 5).

3.1. The method of separation

The EPS depend not only on the frequency ω but also on spatial state variables. In cases of separable or approximately separable EPS, which as demonstrated in Schillinger and Papadopoulos (2010) is definitely the case of geometric imperfections such as the CNT waviness, the corresponding EPS can be expressed as the product of a homogeneous power spectrum $S_h(\omega)$ and a spatial envelope function $g_h(x)$ as follows:

$$S(\omega, x) = S_h(\omega) \cdot g_h(x) \tag{9}$$

Various methodologies have been proposed in the past for estimating EPS from available experimental measurements, i.e., from real samples of stochastic signals. Among them the most widely used are the short-time Fourier transform and the wavelet-based EPS estimation (Cohen, 1995; Mallat, 1999; Newland, 1994a,b; Spanos et al., 2005). The basic disadvantage of these approaches is that they cannot achieve simultaneous resolution in space and frequency domains. A novel methodology was proposed in Schillinger and Papadopoulos (2010) to obtain estimates of EPS of separable processes. This method is based on simple principles of stochastic process theory and for this reason it is easy to implement as well as computationally efficient, while at the same time proved to be accurate enough with optimum simultaneous resolution in space and frequency (Broggi and Schuëller, 2011; Schillinger and Papadopoulos, 2010; Schillinger et al., 2010).

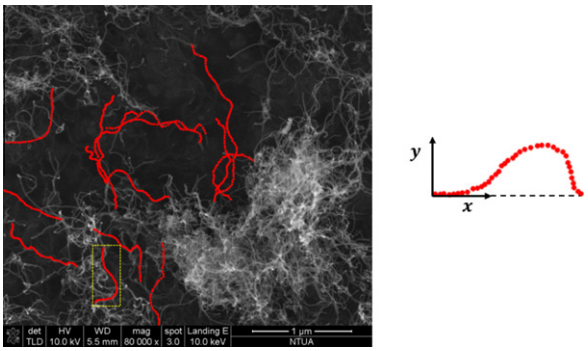

Fig. 5. SEM image and processing of wavy geometry of selected CNTs.

According to this approach an estimate of the first term in Eq. (9) can be readily obtained by averaging the periodograms over the ensemble:

$$\bar{S}_h(\omega) = E\left[\frac{1}{2\pi L}\left|\int_0^L f^{(i)}(x) \cdot e^{-i\omega x} dx\right|^2\right] \tag{10}$$

where $f^{(i)}(x)$ is a sample of the stochastic field (in particular the wavy geometry of the ith CNT) and $E[\cdot]$ denotes the mathematical expectation. An estimate of the spatial envelope function can be obtained from the distribution of the mean square over the samples as follows:

$$\bar{g}_h(x) = \frac{E\left[|f(x)|^2\right]}{2\int_0^\infty \bar{S}_h(\omega) d\omega} \tag{11}$$

It can be easily shown that an unbiased estimate of the evolutionary power spectra may be obtained as follows:

$$\bar{S}_h(\omega,x) = E\left[\left|f^{(i)}(x)\right|^2\right]\frac{\bar{S}_h(\omega)}{2\int_0^\infty \bar{S}_h(\omega)d\omega} \tag{12}$$

Having estimated the EPS from a number of selected CNTs taken from Fig. 5 samples of wavy CNTs can be generated using Eq. (12) for the spectral representation method, as follows:

$$\hat{f}^{(j)}(x) = \sqrt{2}\sum_{n=0}^{N-1} A_n \cos(\omega_n x + \varphi_n^{(j)}) \tag{13}$$

where

$$\begin{aligned} &A_n = \sqrt{2\bar{S}_h(\omega_n,x)\Delta\omega}, \quad n = 0,1,\ldots,N-1\\ &\omega_n = n\Delta\omega, \quad n = 0,1,\ldots,N-1\\ &\Delta\omega = \frac{\omega_{up}}{N}\\ &A_0 = 0, \bar{S}_h(\omega_0,x) = 0 \end{aligned} \tag{14}$$

The parameter ω_{up} refers to an upper limit of the frequency, beyond which the autocorrelation function is supposed to be zero. Parameter $\varphi_n^{(j)}$ stands for random phase angles in the range [0–2π], for the jth sample realization.

Fig. 6 presents the EPS estimated from Eq. (12), while sample realizations of the CNTs with wavy geometry generated using Eq. (13), is plotted in Fig. 7. As can be seen in this figure, a 3D spatial waviness is considered by assuming that the coordinates $z = z(x)$ and $y = y(x)$ of the CNT are independent stochastic fields generated from Eq. (13).

4. Viscoelastic modeling of PEEK

The viscoelastic material used for the polymer is the semi-crystalline thermoplastic polymer poly-ether–ether-ketone (PEEK). This polymer due to its superior mechanical properties (Jones et al., 1985; Searle and Pfeiffer, 1985), such as high strength, modulus and toughness, combined with its excellent thermal stability and chemical resistance becomes highly suitable for high-performance composite materials. The viscoelastic behavior of PEEK is rather complex, so a more complicated numerical model than a simple spring and a dashpot is required for its simulation. Such model is the Maxwell–Wiechert model which accounts for a distribution of relaxation times in a viscoelastic material response (Kaliske and Rothert, 1997). It is consisted by a finite number of separate

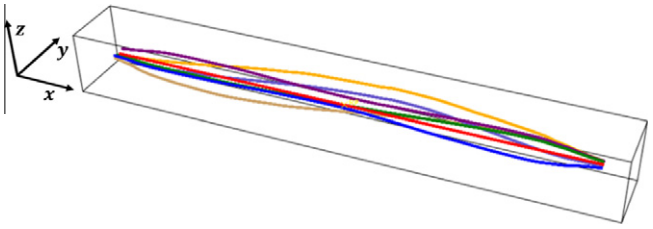

Fig. 7. Sample realizations of wavy CNTs.

Maxwell-elements and an elastic Hooke-element connected in parallel, as depicted in Fig. 8.

The stress–strain relation for this model is given by

$$\hat{\sigma}(t) = E_\infty\hat{\varepsilon}(0) + \sum_{j=1}^{N} E_j \exp\left(-\frac{t}{\tau_j}\right)\hat{\varepsilon}(0) \tag{15}$$

where $\tau_j = n_j/E_j$ are the various relaxation times, related to the viscocity parameters n_j and the elastic spring constants E_j.

4.1. Viscoelastic material characterization

A useful tool in viscoelastic material characterization is the dynamic mechanical analysis (DMA) test in conjunction with a time–temperature correspondence principle. By this experimental tool viscoelastic data is determined over a limited range of time or frequency, but within a large range of temperatures. Master curves derived by the above experimental procedure are used for parameter identification of the viscoelastic models. Using a nonlinear least-squares fit the unknown relaxation times τ_j and the elastic spring constants E_j are determined from the experimental master curves of a specific viscoelastic material. The error function which has to be minimized is

$$R^2 = \sum_{i=1}^{M}\frac{1}{\hat{\Gamma}_\infty^2}\left[(\Gamma' - \bar{\Gamma}')_i^2 + (\Gamma'' - \bar{\Gamma}'')_i^2\right] \tag{16}$$

where Γ' and Γ'' are the storage and loss modulus values of PEEK predicted by the model, while $\bar{\Gamma}'$ and $\bar{\Gamma}''$ are their experimental data measured at M values of frequency.

Master curves of PEEK derived from corresponding DMA tests are illustrated in Figs. 9 and 10 where the tensile storage and loss

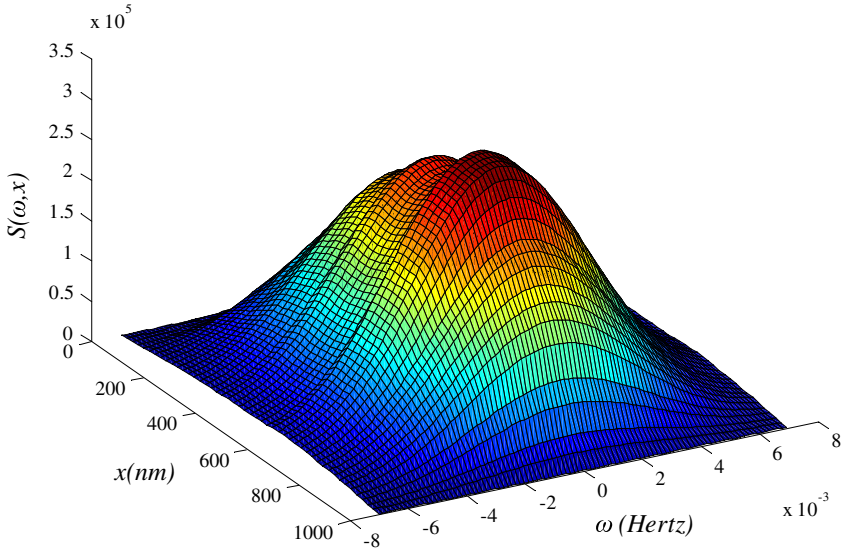

Fig. 6. EPS derived from SEM image.

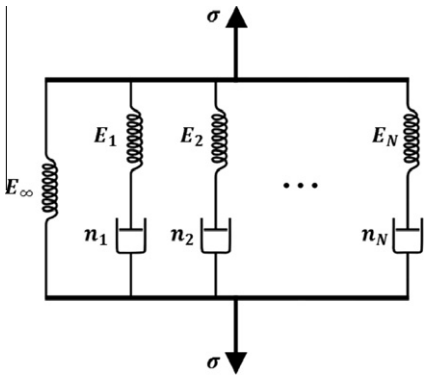

Fig. 8. The Maxwell–Wiechert model.

modulus are depicted with respect to frequency in a log–log diagram. The instantaneous Young's modulus of PEEK can be obtained from the tensile storage modulus value corresponding to the highest frequency and it is found to be approximately 3 MPa (NTUA-C, MRECT report M18). For comparison reasons the corresponding numerical curves are also plotted. The parameters of the Maxwell–Wiechert model derived after minimization of the error function in Eq. (16) are presented in Table 1. The nonlinear least square fitting algorithm resulted in 12 Maxwell elements. Their contribution to the material's response is also depicted in Figs. 9 and 10. Notice that parameter identification is conducted on the basis of the storage modulus $\bar{\Gamma}'$ which unavoidably leads to some discrepancies between numerical and experimental curves for the loss modulus $\bar{\Gamma}''$.

5. Modeling RVEs of CNT-RCs

5.1. The embedded element technique

To avoid complicated mesh discretization in the FEM analysis of the CNT-RCs the embedded element technique is used. The EBE stiffness matrix is calculated in global coordinate system by the equation:

$$K^B = T^T k^b T = T^T \left[\int_{V_e} B^T D B dV_e \right] T \tag{17}$$

where T is the transformation matrix with the kinematic constraints, k^b is the beam's local stiffness matrix, D is the material tensor and B contains derivatives of beam shape functions connecting strains to beam's displacements and rotations. When the beam considered embedded for example in the 8 noded solid finite element (Fig. 11), its translation degrees of freedom can be related to the nodal displacements of the parent solid element according to the following equation:

$$\begin{bmatrix} u_i \\ u_j \\ v_i \\ v_j \\ w_i \\ w_j \end{bmatrix} = \begin{bmatrix} N^M & O & O \\ O & N^M & O \\ O & O & N^M \end{bmatrix} \begin{bmatrix} U^M \\ V^M \\ W^M \end{bmatrix} \tag{18}$$

where

$$N^M = \begin{bmatrix} N_{1(i)} \cdots N_{8(i)} \\ N_{1(j)} \cdots N_{8(j)} \end{bmatrix} \tag{19}$$

are the shape functions of the solid element evaluated at points i and j where beam's nodes lying (Fig. 11).

$$U^M = [U_1 \cdots U_8]^T, \quad V^M = [V_1 \cdots V_8]^T, \quad W^M = [W_1 \cdots W_8]^T \tag{20}$$

are the nodal displacements of the host solid element.

Modifying the deformation matrix B in Eq. (17) to account for the relation Eq. (18), we derive an extended matrix (30×30) for beam's stiffness $\bar{K}^B$, relating 24 translations $[U^M, V^M, W^M]$ of the parent element and 6 rotations $[\theta_{Xi}, \theta_{Yi}, \theta_{Zi}, \theta_{Xj}, \theta_{Yj}, \theta_{Zj}]$ of the beam with external nodal forces and moments, respectively. The final stiffness matrix assemblage resulting from the parent solid element and the embedded beam can be formulated as:

$$K_{(30\times30)} = \begin{bmatrix} K^M + \bar{K}^B_{TT} & \bar{K}^B_{TR} \\ \bar{K}^B_{RT} & \bar{K}^B_{RR} \end{bmatrix} \tag{21}$$

where K^M is the stiffness matrix of the solid element, $\bar{K}^B_{TT}$ stands for the extended stiffness matrix of the beam related only to the

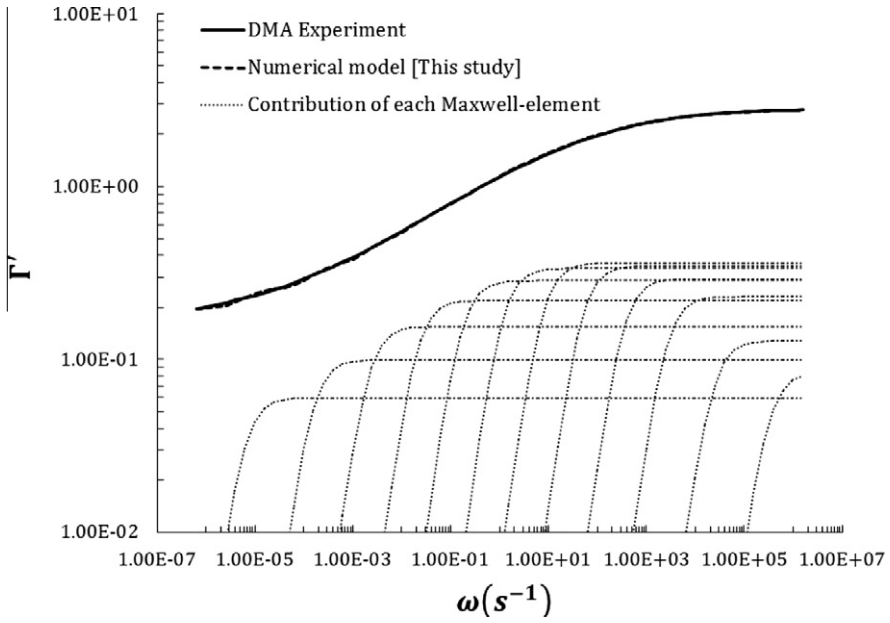

Fig. 9. Storage modulus: experimental master curve vs. mathematical model.

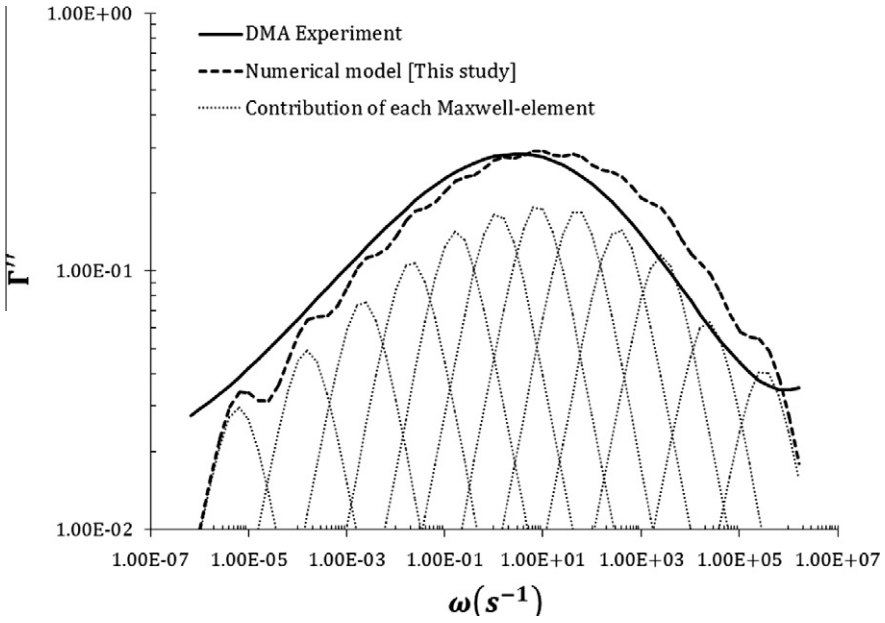

Fig. 10. Loss Modulus: experimental master curve vs. mathematical model.

Table 1
Parameters of Maxwell–Wiechert model for PEEK.

j	E_j [MPa]	τ_j	j	E_j [MPa]	τ_j	j	E_j [MPa]	τ_j
1	8.31E−02	1.42E−06	5	3.47E−01	8.85E−03	9	2.19E−01	2.12E+01
2	1.28E−01	1.96E−05	6	3.60E−01	5.78E−02	10	1.54E−01	2.09E+02
3	2.29E−01	1.74E−04	7	3.35E−01	3.77E−01	11	9.91E−02	2.88E+03
4	2.92E−01	1.30E−03	8	2.84E−01	2.65E+00	12	5.97E−02	7.16E+04

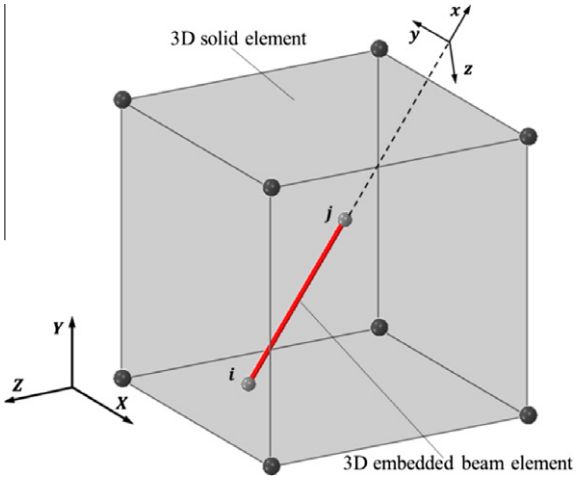

Fig. 11. Illustration of the embedded beam element.

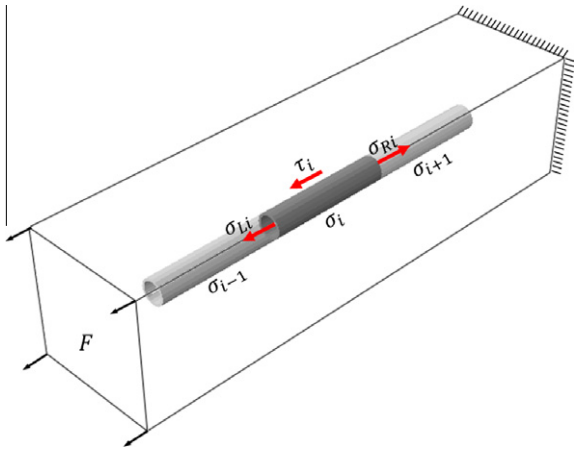

Fig. 12. Stress states on reinforcement beams in a RVE in tension.

translation degrees of freedom, $\bar{K}^{B}_{RR}$ is accordingly related only to the rotation dof and $\bar{K}^{B}_{TR}$ and $\bar{K}^{B}_{RT}$ contain the interaction terms for the translation and rotation dof respectively.

5.2. Bond-slip model

Mechanical and damping properties of the nanocomposites are sensitive to the interfacial characteristics between the CNT and the matrix. Loads are transferred from the polymer to the CNTs through their interface. Experimental evidence (Ramanathan et al., 2005; Velasco-Santos et al., 2003; Zhu et al., 2003) demonstrated that if functionalization techniques are applied on the surface of carbon nanotubes, higher ISS may be achieved leading to improved stiffness and damping properties of the CNT-RCs, while high aspect ratio of CNTs enhances this load transfer mechanism.

Pullout tests (Yogeeswaran, 2011; Barber et al., 2003; Qian et al., 2000; Schadler et al., 1998) on CNT-RCs revealed a stick–slip behavior of the nanotube inside the matrix. For this reason, a non-linear friction-type bond-slip model is incorporated in the mulit-scale analysis described in Section 2. This model was first implemented in the commercial FEA program ATENA (http://www.cervenka.cz/products/atena/) where it is used to describe cohesion between reinforcement bar and concrete. Phenomenologically the nanoscale CNT-RC problem is similar to the mesoscale

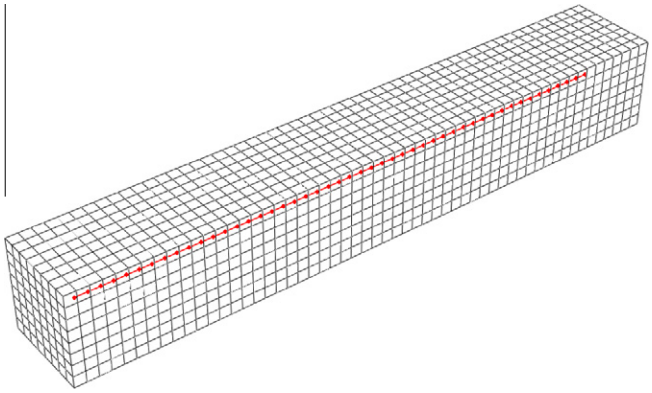

Fig. 13. Mesh of the RVE with a straight CNT.

problem of any fiber-reinforced composite material such as reinforced concrete. The adopted solution is fairly simple and provides reasonable accuracy at low computation cost. Fig. 12 depicts a RVE consisted of a straight CNT modeled with three EBEs of pipe section profile which are embedded in the polymer discretized with solid finite elements. The equilibrium equation for the central EBE can be written as:

$$|\sigma_{Ri} - \sigma_{Li}|A_i = \tau_i \pi (D_i + t_i) l_i \tag{22}$$

where A_i is the cross sectional area of the beam which has an outer diameter $D_i + t_i$ and l_i is the beam's length. The nodal axial stresses σ_{Ri} and σ_{Li} acting on right and left end section of the beam are derived after a smoothing operation as:

$$\sigma_{Ri} = \frac{\sigma_i l_i + \sigma_{i+1} l_{i+1}}{l_i + l_{i+1}} \tag{23}$$

$$\sigma_{Li} = \frac{\sigma_i l_i + \sigma_{i-1} l_{i-1}}{l_i + l_{i-1}} \tag{24}$$

Solving Eq. (22) for τ_i we obtain the shear stress at the interface between the CNT and the matrix. Comparing this value to the interfacial shear strength (ISS), a bond slip friction-type model is implemented in the form:

$$\tau_i = \frac{A_i}{\pi (D_i + t_i) l_i} |\sigma_{Ri} - \sigma_{Li}| \begin{cases} < ISS \ \ fully \ bonded \\ \geqslant ISS \ \ slip \end{cases} \tag{25}$$

If an EBE, representing some portion of the full length CNT, is in slip state, this means that its corresponding interface bond has failed, leading to its inability for further load-transferring. The condition of slip for a beam element is simulated by reducing its axial stiffness to a very small value. Notice that bending and torsion rigidities are not affected allowing the element in slip to resist against bending and torsion.

The above procedure is implemented within a full Newton–Raphson incremental-iterative scheme, used for the solution of the resulted nonlinear equations, as follows:

Step 1: Compute the incremental displacements ${}^t\Delta u^{(i)}$ at increment t and iteration i due to the increment ${}^t\Delta P$ of the external load vector

$${}^t\Delta u^{(i)} = \left[{}^tK_T^{(i)} \right]^{-1} {}^t\Delta P \tag{26}$$

where ${}^tK_T^{(i)}$ is the global tangent stiffness matrix of the RVE model.

Step 2: Loop over all beam elements and check each element e for slippage

$$\text{Slippage} \begin{cases} \text{no} \rightarrow \ {}^tK_{Te}^{(i)} = {}^tK_{Te}^{(i-1)} \\ \text{yes} \rightarrow {}^tK_{Te}^{(i)} = {}^tK_{Te}^{(i-1)} \ \text{with} \ \ (EA)_e \rightarrow 0 \end{cases} \tag{27}$$

when slippage occurs, the axial stiffness is reduced to zero resulting in a local modified tangent stiffness matrix ${}^tK_{Te}^{(i)}$.

Step 3: Correction of internal forces ${}^t\Delta F_e^{(i)}$ of element e and update global force vector ${}^tF^{(i)}$

$${}^t\Delta F_e^{(i)} = {}^tK_{Te}^{(i)} {}^t\Delta u_e^{(i)} \tag{28a}$$

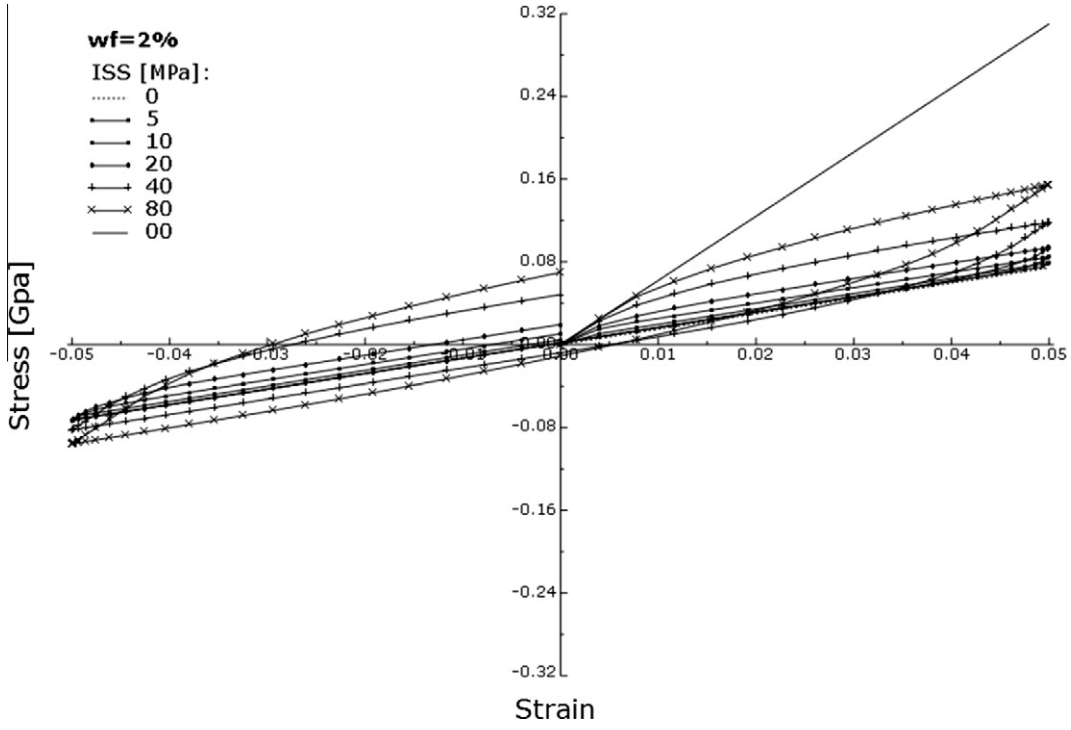

Fig. 14. Stress–strain curves for CNT-RC RVEs considering linear elastic polymer with wf ≈ 2% and ISS = 0, 5, 10, 20, 40, 80 and ∞ MPa.

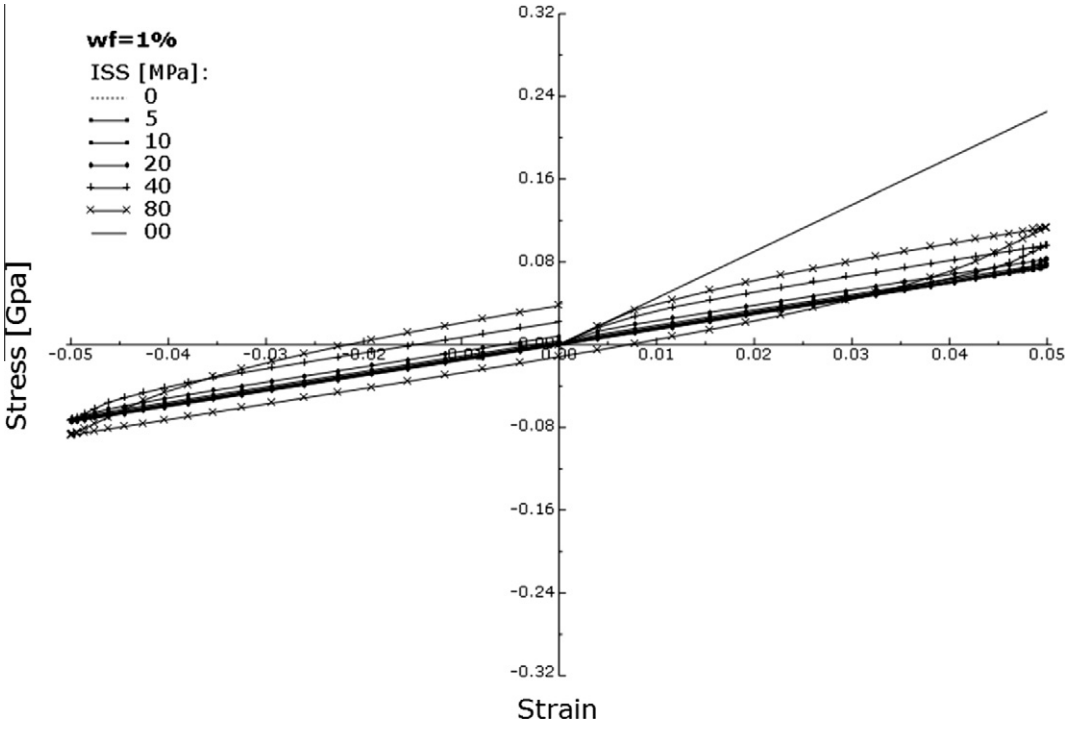

Fig. 15. Stress–strain curves for CNT-RC RVEs considering linear elastic polymer with wf ≈ 1% and ISS = 0, 5, 10, 20, 40, 80 and ∞ MPa.

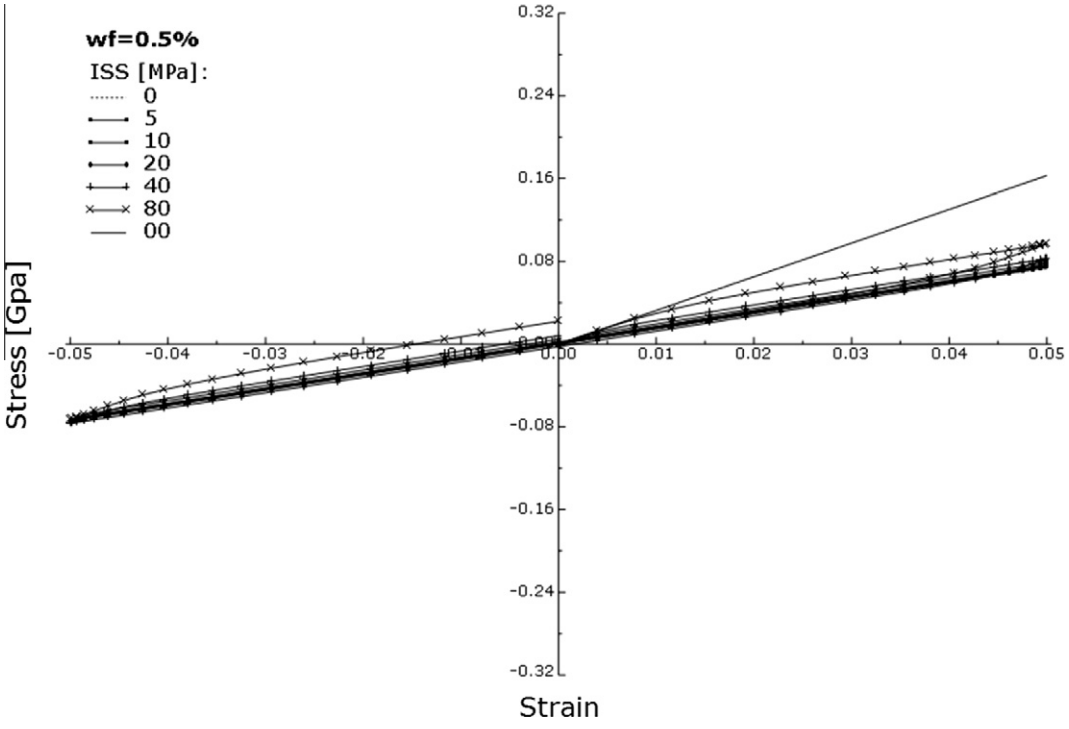

Fig. 16. Stress–strain curves for CNT-RC RVEs considering linear elastic polymer with wf ≈ 0.5% and ISS = 0, 5, 10, 20, 40, 80 and ∞ MPa.

$$ {}^{t}F^{(i)} = {}^{t}F^{(i-1)} + \sum_{e=1}^{N} {}^{t}\Delta F_e^{(i)} \tag{28b} $$

Step 4: Compute the residuals ${}^{t}r^{(i)}$

$$ {}^{t}r^{(i)} = {}^{t}P - {}^{t}F^{(i)} \begin{cases} \leqslant \text{tol then } t = t+1 \text{ go to next increment} \\ > \text{tol then } i = i+1 \text{ go to STEP 1} \end{cases} \tag{29} $$

6. Numerical results

6.1. Straight CNTs

In the subsequent applications, MWCNTs are used with a nominal outer diameter of 14 nm corresponding to the outer CNT of chirality type armchair (100,100). Using the procedure described in Section 2.2, the MMSM space frame model of this CNT is reduced

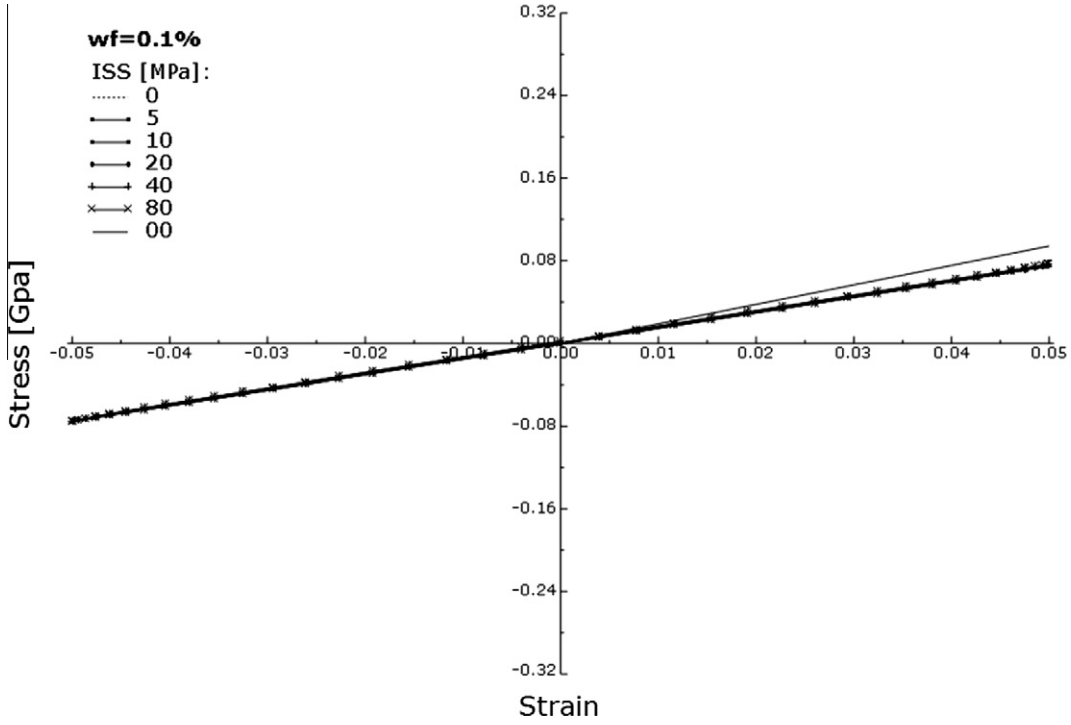

Fig. 17. Stress–strain curves for CNT-RC RVEs considering linear elastic polymer with wf ≈ 0.1% and ISS = 0, 5, 10, 20, 40, 80 and ∞ MPa.

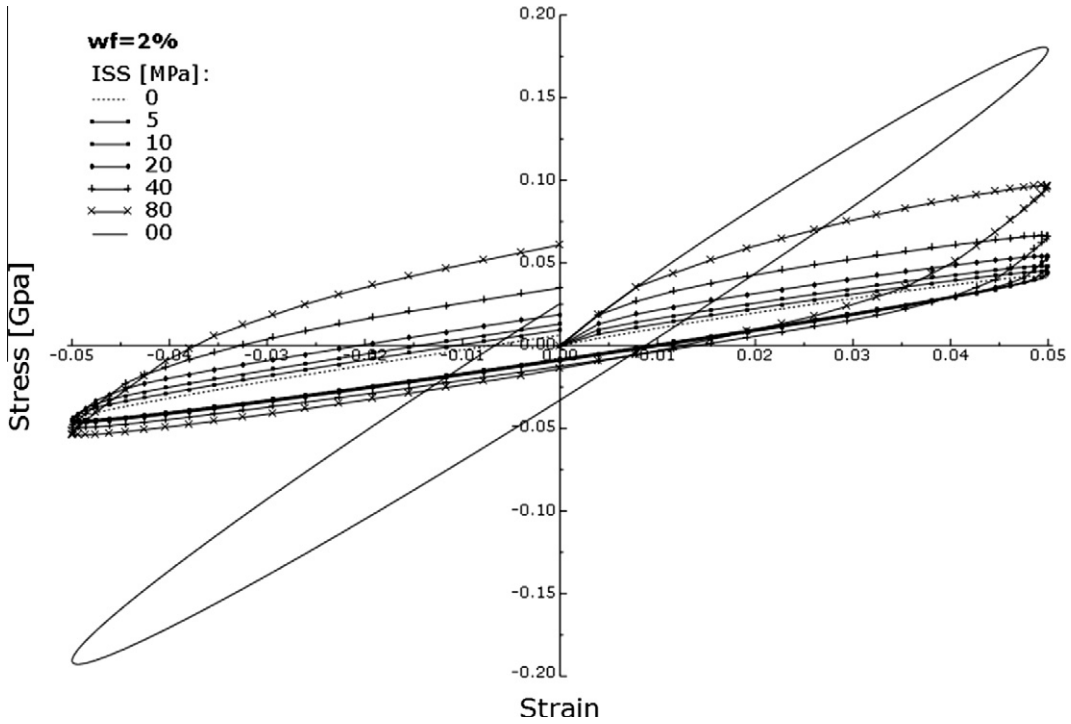

Fig. 18. Stress–strain curves for CNT-RC RVEs considering linear viscoelastic polymer with wf ≈ 2% and ISS = 0, 5, 10, 20, 40, 80 and ∞ MPa.

to a linear EBE with a pipe profile section with wall thickness $t = 0.34$ nm and a mean equivalent diameter computed from Eq. (8) at $d_{eq} \approx 13.453$ nm. Equivalent Young's and shear moduli were calculated from Eqs. (1)–(3) at $E \approx 1.051$ TPa and $G \approx 0.503$ TPa, respectively. RVEs with CNT weight fractions (wfs) ranging from 0.1% to 2% were analyzed in monotonic as well as cyclic axial loading with 1 Hz frequency and strain amplitude 5%. Despite the fact that the RVEs are strained up to 5%, CNT-polymer slippage occurs at a much earlier stage which can be observed at Figs. 14–21. As a result, the CNTs are strained less than 1% for all the considered cases, leading thus to a reasonable linear elastic assumption for the CNTs. The RVE FE model is illustrated at Fig. 13. The effect of the ISS on both stiffness and damping properties of the CNT-RCs were assessed through parametric studies conducted for various values of the ISS parameter of the bond-slip model in Section 4, ranging from 5 to 80 MPa. Notice that the tensile elongation of

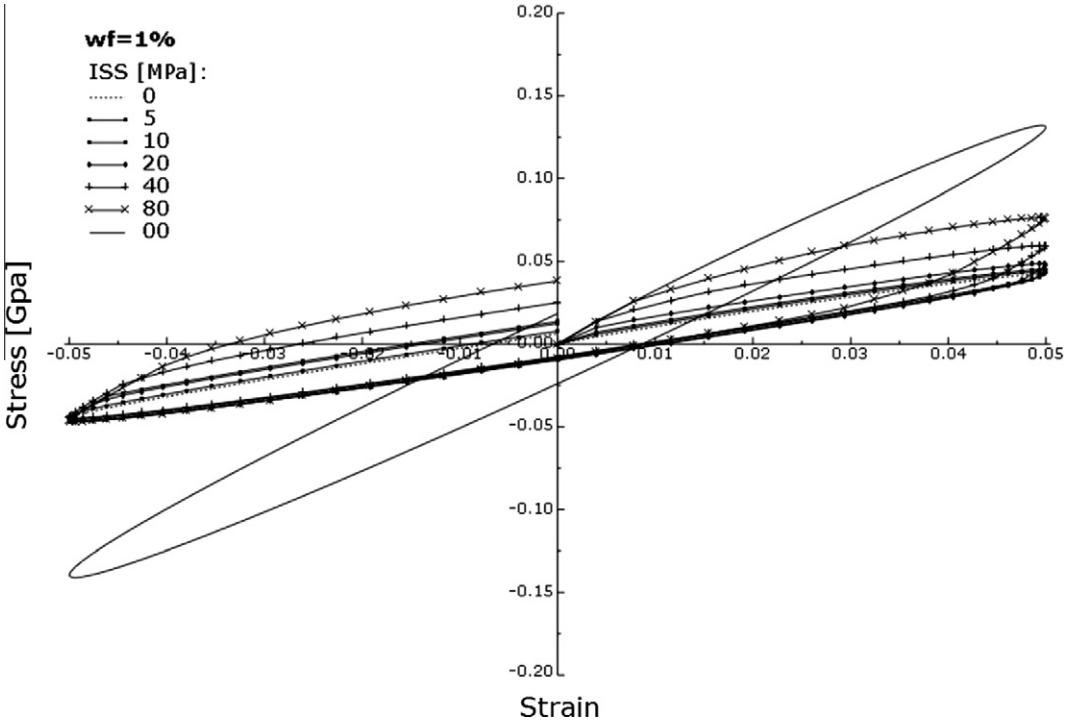

Fig. 19. Stress–strain curves for CNT-RC RVEs considering linear viscoelastic polymer with wf ≈ 1% and ISS = 0, 5, 10, 20, 40, 80 and ∞ MPa.

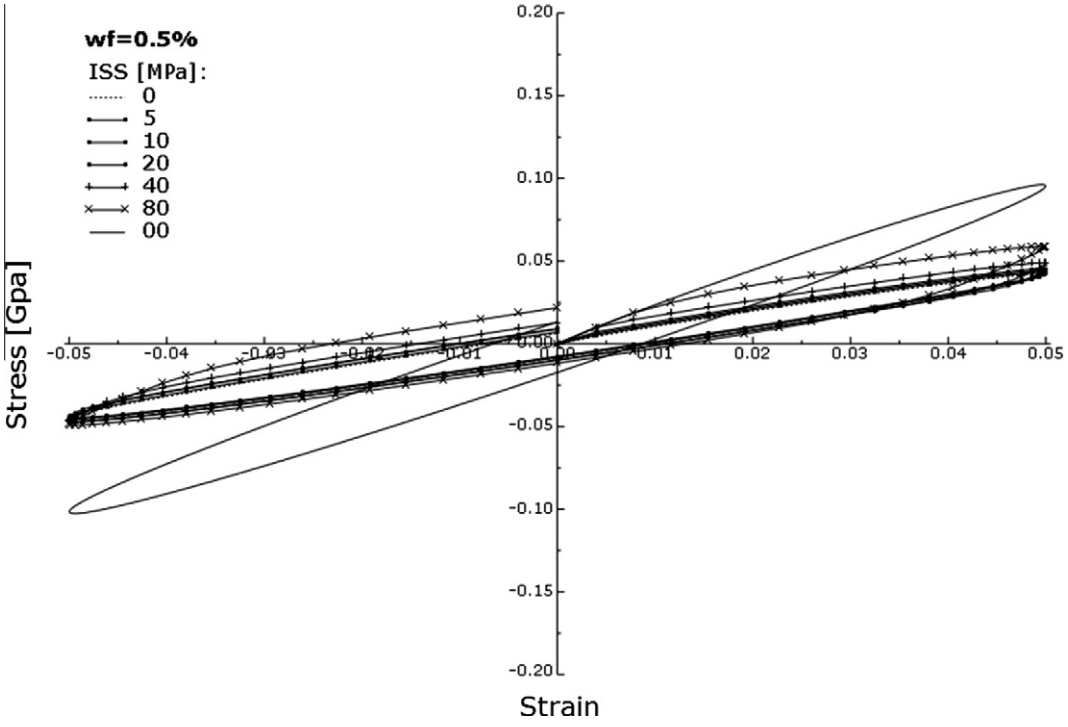

Fig. 20. Stress–strain curves for CNT-RC RVEs considering linear viscoelastic polymer with wf ≈ 0.5% and ISS = 0, 5, 10, 20, 40, 80 and ∞ MPa.

PEEK polymer at yield point is 5% and its shear strength is 53 MPa (http://www.victrex.com).

Figs. 14–17 present the computed stress–strain diagrams for five different values of the ISS (ISS = 5, 10, 20, 40 and 80 MPa) as well as the fully bonded model (ISS = ∞) and the neat PEEK (ISS = 0) for CNT weight fractions wf ≈ 2%, 1%, 0.5% and 0.1%, respectively. The polymer in all above cases is assumed as purely elastic. The energy dissipation under cyclic loading in these figures is attributed only to CNT slippage along its interface with the polymer. From these figures it can be observed that in all cases, the stiffness and the energy dissipation capability of the CNT-RC is increased with increasing ISS, while the overall stiffness approaches the stiffness of the fully bonded case, which reaches 3 times the stiffness of the neat PEEK for a wf ≈ 2%. A wf ≈ 0.1% marginally influences the behavior of neat PEEK.

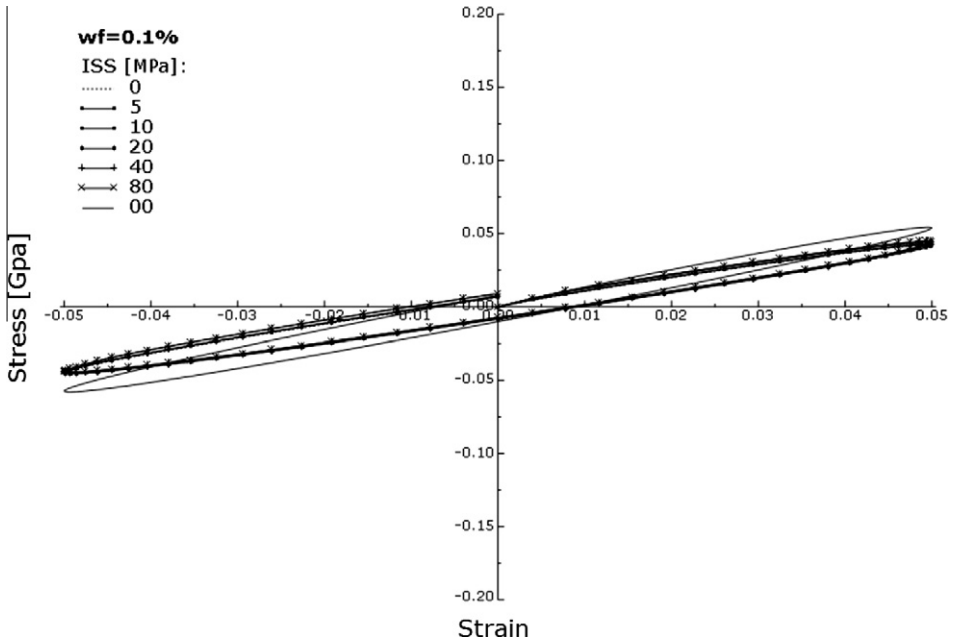

Fig. 21. Stress–strain curves for CNT-RC RVEs considering linear viscoelastic polymer with wf ≈ 0.1% and ISS = 0, 5, 10, 20, 40, 80 and ∞ MPa.

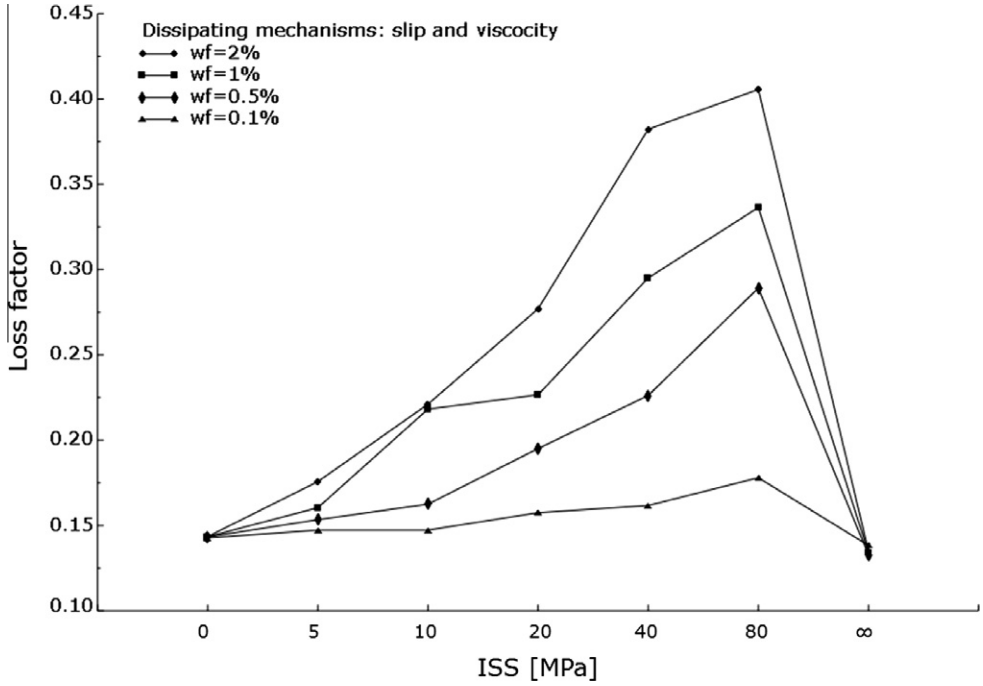

Fig. 22. Loss factor computed from the hysteresis loop of CNT-RC RVEs considering linear viscoelastic polymer for wf = 2, 1, 0.5, 0.1% and ISS = 0, 5, 10, 20, 40, 80 and ∞ MPa.

Figs. 18–21 present the same results with Figs. 14–17, but for a viscoelastic behavior of the polymer. The energy dissipation under cyclic loading in these figures is attributed to both the viscoelastic matrix and the CNT slippage along its interface with the polymer. From these figures it can also be observed that in all weight fractions, the energy dissipation capability of the CNT-RC is increased for increasing ISS, while the overall stiffness approaches the stiffness of the fully bonded case. The energy dissipation characteristics are more pronounced for weight fractions larger than 0.5% while relatively small weight fractions of the order of 0.1% exhibit a damping behavior very similar to that of the neat PEEK material.

Fig. 22 presents the effective loss factor as a function of the various ISS values (5, 10, 20, 40 and 80 MPa) and weight fractions (wf ≈ 2, 1, 0.5 and 0.1%) for linear viscoelastic polymer (PEEK). The loss factor values for the case of neat PEEK (ISS = 0) and for the fully bonded case (ISS = ∞) are also depicted. The effective loss factor is computed as the ratio of the dissipated energy per unit volume to the maximum stored energy per unit volume expressed by

$$\tan\delta = \frac{D}{\pi\sigma_0\varepsilon_0} \tag{30}$$

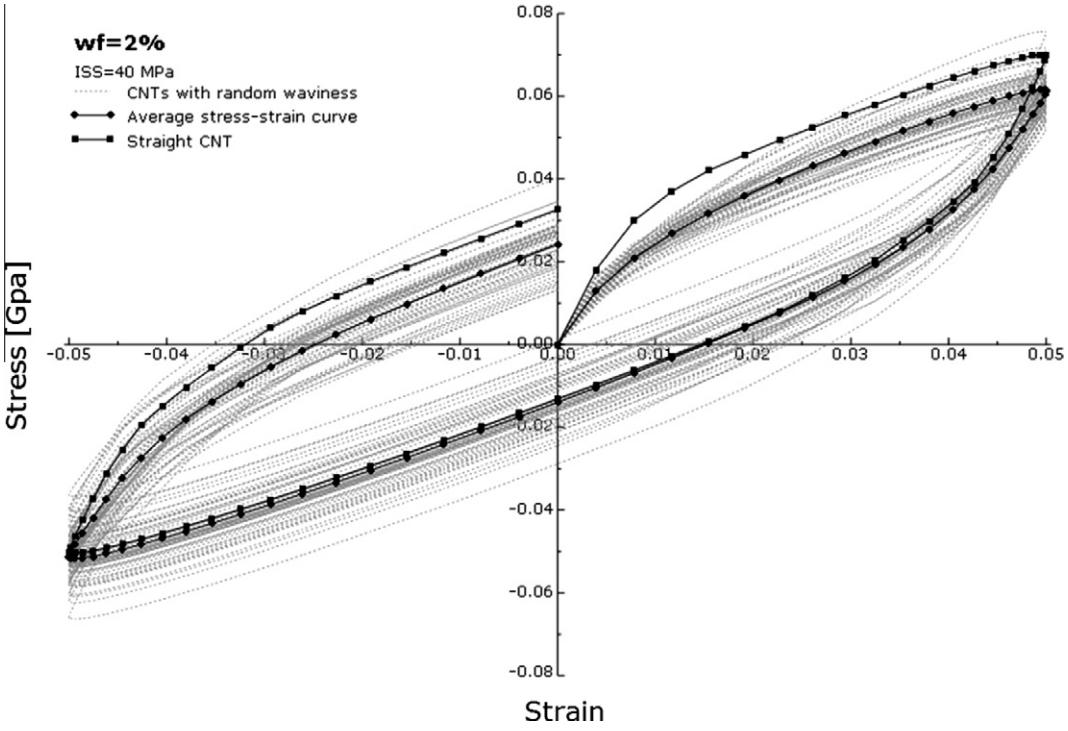

Fig. 23. Comparison between average stress–strain curve of 50 RVEs with random wavy CNTs with the corresponding RVE with a straight CNT (wf = 2% and ISS = 40 MPa).

where σ_0 and ε_0 are the mean stress and strain amplitudes obtained from the finite element analysis of the RVE model subjected to cyclic load and D is the area captured within the hysteresis stress–strain loop corresponding to the dissipated energy per cycle. This figure quantifies the previously mentioned observation that the energy dissipation capacity of the CNT-RC is increased for increasing ISS. The loss factor increases with increasing ISS and reaches a maximum plateau for values greater than 40 MPa which are values that are equal or greater than the shear strength of the PEEK (52 MPa). The maximum loss factor reached for ISS = 80 MPa is more than 200%, 250% and 300% the loss factor of neat PEEK for wfs $\approx$ 0.5, 1% and 2%, respectively. This increase, however, is marginal in the case of small weight fractions in the order of wf = 0.1%. In all cases, the loss factor decreases after this maximum plateau (for values of the ISS larger than 80 Mpa), reaching the loss factor of the full-bond condition. This behavior of the CNT-RCs implies that a successful functionalization process capable of producing an increased ISS, close or slightly higher than the corresponding shear strength of the polymer, is crucial for achieving optimum damping characteristics. Notice that as CNTs content is increased the stiffness of the RVE is increased too, leading to the reduction of the loss factor. This fact can be observed in Fig. 22 especially for the fully bonded case (ISS = ∞). However as wf is increased the total area of the lateral surface of CNTs is increased too, leading to a reduction of the interfacial shear stresses under the same external loads on the RVE. This means that the RVE can reach higher stresses before the critical ISS value is exceeded and subsequently slip occurs. This delay of slip causes an increased hysteresis loop in the stress–strain diagram of the RVE. Notice that in all simulations the strain amplitude is constant (±5%) as the RVE model is subjected to a prescribed cyclic deformation. For ISS values higher than 80 MPa the loss factor is decreasing as the fully bonded state and the high stiffness of the RVE start to dominate.

6.2. Wavy CNTs

Stochastic analysis is performed as a next step to account for the random CNT waviness. For this purpose, a number of random CNT geometries were generated using Eq. (13) and the corresponding RVE FE models with wf $\approx$ 2% were analyzed in the context of a Monte Carlo simulation for cyclic loading and ISS = 40 MPa. From the cloud of the computed stress–strain curves presented in Fig. 23, the average curve was estimated. This average curve, together with the stress–strain curve corresponding to a RVE with a straight CNT, is also depicted in Fig. 23 for comparison purposes. It must be mentioned that CNT length is the same in all RVE models, so the observed differences in the stress–strain curves are exclusively attributed to CNT stochastic waviness. From these curves, the values of the loss factor were obtained for the case of wavy and straight CNTs and presented in Table 2 where it can be seen that CNT waviness results in a 15% reduction of loss factor. So we can conclude that CNTs straightening is important, leading to improved damping properties of the CNT-RCs.

Table 2
Loss factor values for straight and wavy CNTs.

	Straight CNT	Wavy CNTs
Loss factor	0.3744	0.3182

7. Conclusions

In the present study the effect of interfacial shear strength on the mechanical and damping properties of CNT-RCs is investigated using a multiscale simulation. The atomic lattice of CNTs is modeled as a space frame structure using the modified molecular structural mechanics approach. Subsequently, this model is reduced to an equivalent beam element which is used as the basic building block for the construction of full length CNTs embedded in the polymer. Linear material properties are assigned to the equivalent beam elements, while a Maxwell–Wiechert material model is used for modeling the viscoelastic behavior of the PEEK polymer. The interfacial load transfer mechanism between the lateral surface

of the CNT and the surrounding matrix is taken into account with a nonlinear bond-slip friction-type model. Straight as well as wavy CNTs were investigated. In the case of wavy CNTs, random CNT geometries are generated using the spectral representation method with evolutionary power spectra derived from processing scanning electron microscope images. Stochastic average properties were derived with Monte Carlo simulation.

From the Numerical results presented, the significant effect of the interfacial shear strength, as well as the influence of CNT waviness on the damping behavior of CNT-RCs, was demonstrated. Specifically it was shown that the loss factor increases with increasing ISS and reaches a maximum plateau for values equal or greater than the shear strength of the polymer. This behavior of the CNT-RCs implies that a successful functionalization process that results in increased interfacial shear strength is crucial for achieving optimum damping characteristics. In addition, it is demonstrated that CNT waviness results in a reduction of loss factor leading to the conclusion that straightening of CNTs is important leading to improved damping properties of the CNT-RCs. Nonlinear phenomena, such as buckling of nanotubes or defected C–C bonds, which would result in an equivalent beam element (EBE) with nonlinear behavior, would be considered by the authors in a future research. Experimental validation of the present numerical results is essential in order to demonstrate the effectiveness of the proposed modeling. To the authors knowledge there is luck of published experimental data concerning damping measurements on CNT-PEEK composites in literature. However in Michelis et al. (2012) experimental results are provided for cyclic tests on CNT-PEEK tapes with wf = 0.5% under constant strain amplitude performed at room temperature, 1 Hz frequency and at different strain levels ranging from well within the elastic domain to large plastic deformations near failure. The measured damping coefficient ranged from 0.3 to 0.56. These values are quite close to the ones predicted numerically in this study.

Acknowledgments

This work has been supported by the European Community FP7 Collaborative Project "M-RECT-Multiscale reinforcement of semi-crystalline thermoplastic sheets and honeycombs" (FP7-NMP-2009-2.5-1) and the European Research Council Advanced Grant "MASTER – Mastering the computational challenges in numerical modeling and optimum design of CNT reinforced composites" (ERC-2011-ADG_20110209). The authors wish also to thank Professor E. Kontou for providing the master curves of PEEK.

References

Agrawal, P.M., Sudalayandi, B.S., Raff, L.M., Komanduri, R., 2008. Molecular dynamics (MD) simulations of the dependence of C–C bond lengths and bond angles on the tensile strain in single-wall carbon nanotubes (SWCNT). Computat. Mater. Sci. 41 (4), 450–456.

Arroyo, M., Belytschko, T., 2004a. Finite crystal elasticity of carbon nanotubes based on the exponential Cauchy–Born rule. Phys. Rev. B – Condens. Matter Mater. Phys. 69 (11), 1154151–11541511.

Arroyo, M., Belytschko, T., 2004b. Finite element methods for the non-linear mechanics of crystalline sheets and nanotubes. Int. J. Numer. Methods Eng. 59 (3), 419–456.

Barber, A.H., Cohen, S.R., Wagner, H.D., 2003. Measurement of carbon nanotube–polymer interfacial strength. Appl. Phys. Lett. 82 (23), 4140–4142.

Broggi, M., Schuëller, G.I., 2011. Efficient modeling of imperfections for buckling analysis of composite cylindrical shells. Eng. Struct. 33 (11), 1796–1806.

Chandraseker, K., Mukherjee, S., 2007. Atomistic-continuum and ab initio estimation of the elastic moduli of single-walled carbon nanotubes. Computat. Mater. Sci. 40 (1), 147–158.

Chang, T., Gao, H., 2003. Size-dependent elastic properties of a single-walled carbon nanotube via a molecular mechanics model. J. Mech. Phys. Solids 51 (6), 1059–1074.

Chen, W.H., Cheng, H.C., Hsu, Y.C., 2007. Mechanical properties of carbon nanotubes using molecular dynamics simulations with the inlayer van der Waals interactions. Comput. Model. Eng. Sci. 20 (2), 123–145.

Chen, W.-H., Cheng, H.C., Liu, Y.-L., 2010. Radial mechanical properties of single-walled carbon nanotubes using modified molecular structure mechanics. Computat. Mater. Sci. 47, 985–993.

Cheng, H.-C., Liu, Y.-L., Hsu, Y.-C., Chen, W.-H., 2009. Atomistic-continuum modeling for mechanical properties of single-walled carbon nanotubes. Int. J. Solids Struct. 46 (7–8), 1695–1704.

Cheng, H.C., Liu, Y.L., Wu, C.H., Chen, W.H., 2010. On radial breathing vibration of carbon nanotubes. Comput. Methods Appl. Mech. Eng. 199, 2820–2827.

Cohen, L., 1995. Time-Frequency Analysis. Prentice Hall, New Jersey.

Demczyk, B.G., Wang, Y.M., Cumings, J., Hetman, M., Han, W., Zettl, A., Ritchie, R.O., 2002. Direct mechanical measurement of the tensile strength and elastic modulus of multiwalled carbon nanotubes. Mater. Sci. Eng., A 334 (1–2), 173–178.

Georgantzinos, S.K., Giannopoulos, G.I., Anifantis, N.K., 2009. Investigation of stress–strain behavior of single walled carbon nanotube/rubber composites by a multi-scale finite element method. Theoret. Appl. Fract. Mech. 52 (3), 158–164.

Hernandez, E., Goze, C., Bernier, P., Rubio, A., 1998. Elastic properties of C and BxCyNz composite nanotubes. Phys. Rev. Lett. 80 (20), 4502–4505.

Hu, N., Nunoya, K., Pan, D., Okabe, T., Fukunaga, H., 2007. Prediction of buckling characteristics of carbon nanotubes. Int. J. Solids Struct. 44 (20), 6535–6550.

Iijima, S., 1991. Helical microtubules of graphitics carbon. Lett. Nature 354, 56–58.

Jin, Y., Yuan, F.G., 2003. Simulation of elastic properties of single-walled carbon nanotubes. Compos. Sci. Technol. 63 (11), 1507–1515.

Jones, D.P., Leach, D.C., Moore, D.R., 1985. Mechanical properties of poly(ether–ether-ketone) for engineering applications. Polymer 26 (9), 1385–1393.

Kaliske, M., Rothert, H., 1997. Formulation and implementation of three-dimensional viscoelasticity at small and finite strains. Comput. Mech. 19, 228–239.

Kudin, K.N., Scuseria, G.E., Yakobson, B.I., 2001. C2F, BN and C nanoshell elasticity from ab initio computations. Phys. Rev. B 64, 235406.

Li, C., Chou, T.-W., 2003a. A structural mechanics approach for the analysis of carbon nanotubes. Int. J. Solid Struct. 40 (10), 2487–2499.

Li, C., Chou, T.-W., 2003b. Elastic moduli of multi-walled carbon nanotubes and the effect of van der Waals forces. Compos. Sci. Technol. 63, 1517–1524.

Lu, J.P., 1997. Elastic properties of carbon nanotubes and nanoropes. Phys. Rev. Lett. 79 (7), 1297–1300.

Lu, W.B., Wu, J., Song, J., Hwang, K.C., Jiang, L.Y., Huang, Y., 2008. A cohesive law for interfaces between multi-wall carbon nanotubes and polymers due to the van der Waals interactions. Comput. Methods Appl. Mech. Eng. 197 (41–42), 3261–3267.

Mallat, S., 1999. A Wavelet Tour of Signal Processing. Academic Press, New York.

Michelis, P., Spitas, V., Spitas, C. 2012. Modelling of the elastic damping response of a carbon nanotube–polymer nanocomposite in the stress–strain domain using an elastic energy release approach based on stick–slip. Mech. Adv. Mater. Struct. http://dx.doi.org/10.1080/15376494.2012.677100.

Nasdala, L., Ernst, G., 2005. Development of a 4-node finite element for the computation of nano-structured materials. Comput. Mater. Sci. 33 (4), 443–458.

Needleman, A., Borders, T.L., Brinson, L.C., Flores, V.M., Schadler, L.S., 2010. Effect of an interphase region on debonding of a CNT reinforced polymer composite. Compos. Sci. Technol. 70 (15), 2207–2215.

Newland, D.E., 1994a. Wavelet analysis of vibration, part I: theory. J. Vibra. Acous. 116, 409–416.

Newland, D.E., 1994b. Wavelet analysis of vibration, Part II: wavelet maps. J. Vibra. Acous. 116, 417–425.

Odegard, G.M., Gates, T.S., Nicholson, L.M., Wise, K.E., 2002. Equivalent continuum modeling of nano-structured materials. Compos. Sci. Technol. 62 (14), 1869–1880.

Pantano, A., Parks, D.M., Boyce, M.C., 2004. Mechanics of deformation of single and multi-wall carbon nanotubes. J. Mech. Phys. Solids 52, 789–821.

Qian, D., Dickey, E.C., Andrews, R., Rantell, T., 2000. Load transfer and deformation mechanisms in carbon nanotube–polystyrene composites. Appl. Phys. Lett. 76 (20), 2868–2870.

Qian, D., Liu, W.K., Zheng, Q., 2008. Concurrent quantum/continuum coupling analysis of nanostructures. Comput. Methods Appl. Mech. Eng. 197 (41–42), 3291–3323.

Ramanathan, T., Liu, H., Brinson, L.C., 2005. Functionalized SWNT/polymer nanocomposites for dramatic property improvement. J. Polym. Sci., Part B: Polym. Phys. 43 (17), 2269–2279.

Salvetat, J.P., Bonard, J.M., Thomson, N.B., Kulik, A.J., Forro, L., Benoit, W., Zuppiroli, L., 1999. Mechanical properties of carbon nanotubes. Appl. Phys. A Mater. Sci. Process. 69 (3), 255–260.

Schadler, L.S., Giannaris, S.C., Ajayan, P.M., 1998. Load transfer in carbon nanotube epoxy composites. Appl. Phys. Lett. 73 (26), 3842–3844.

Schillinger, D., Papadopoulos, V., 2010. Accurate estimation of evolutionary power spectra for strongly narrow-band random fields. Comput. Methods Appl. Mech. Eng. 199 (17–20), 947–960.

Schillinger, D., Papadopoulos, V., Bischoff, M., Papadrakakis, M., 2010. Buckling analysis of imperfect I-section beam-columns with stochastic shell finite elements. Computat. Mech. 46 (3), 495–510.

Searle, O.B., Pfeiffer, R.H., 1985. Victrex poly(ethersulfone) (PES) and Victrex poly(ether ether ketone) (PEEK). Polym. Eng. Sci. 25 (8), 474–476.

Spanos, P.D., Tezcan, J., Tratskas, P., 2005. Stochastic processes evolutionary spectrum estimation via harmonic wavelets. Comput. Methods Appl. Mech. Eng. 194, 1367–1383.

Tan, H., Jiang, L.Y., Huang, Y., Liu, B., Hwang, K.C., 2007. The effect of van der Waals-based interface cohesive law on carbon nanotube-reinforced composite materials. Compos. Sci. Technol. 67 (14), 2941–2946.

Thostenson, E.T., Chou, T.-W., 2003. On the elastic properties of carbon nanotube-based composites: modelling and characterization. J. Phys. D Appl. Phys. 36 (5), 573–582.

Treacy, M.M.J., Ebbesen, T.W., Gibson, J.M., 1996. Exceptionally high Young's modulus observed for individual carbon nanotubes. Nature 381 (6584), 678–680.

Tserpes, K.I., Papanikos, P., Labeas, G., Pantelakis, Sp. G., 2008. Multi-scale modeling of tensile behavior of carbon nanotube-reinforced composites. Theor. Appl. Fract. Mech. 49 (1), 51–60.

Tserpes, K.I., Papanikos, P., Tsirkas, S.A., 2006. A progressive fracture model for carbon nanotubes. Compos. B Eng. 37 (7–8), 662–669.

Tu, Z., Ou-Yang, Z., 2002. Single-walled and multiwalled carbon nanotubes viewed as elastic tubes with the effective Young's moduli dependent on layer number. Phys. Rev. B 65, 233407.

Van Lier, G., Van Alsenoy, C., Van Doren, V., Geerlings, P., 2000. Ab initio study of the elastic properties of single-walled carbon nanotubes and graphene. Chem. Phys. Lett. 326 (1–2), 181–185.

Velasco-Santos, C., Martinez-Hernandez, A.L., Fisher, F.T., Ruoff, R., Castano, V.M., 2003. Improvement of thermal and mechanical properties of carbon nanotube composites through chemical functionalization. Chem. Mater. 15 (23), 4470–4475.

Wernik, J.M., Meguid, S.A., 2009. Coupling atomistics and continuum in solids: status, prospects, and challenges. Int. J. Mech. Mater. Des. 5 (1), 79–110.

Yakobson, B.I., Brabec, C.J., Bernholc, J., 1996. Nanomechanics of carbon tubes: instabilities beyond linear range. Phys. Rev. Lett. 76, 2511–2514.

Yogeeswaran, G., 2011. Interface toughness of carbon nanotube reinforced epoxy composites. Appl. Mater. Interf. Lett. 3, 129–134.

Yu, M.-F., Lourie, O., Dyer, M.J., Moloni, K., Kelly, T.F., Ruoff, R.S., 2000. Strength and breaking mechanism of multiwalled carbon nanotubes under tensile load. Science 287 (5453), 637–640.

Zhou, G., Duan, W., Gu, B., 2001. First-principles study on morphology and mechanical properties of single-walled carbon nanotube. Chem. Phys. Lett. 333 (5), 344–349.

Zhou, X., Zhou, J.J., Ou-Yang, Z.C., 2000. Strain energy and Young's modulus of single-wall carbon nanotubes calculated from electronic energy band theory. Phys. Rev. B 62 (20), 13692–13696.

Zhu, J., Kim, J., Peng, H., Margrave, J.L., Khabashesku, V.N., Barrera, E.V., 2003. Improving the dispersion and integration of single-walled carbon nanotubes in epoxy composites through functionalization. Nano Lett. 3 (8), 1107–1113.